

1 **Retrieval of Cloud Fraction using Machine Learning Algorithms**
2 **based on FY4A AGRI observations.**

3 Jinyi Xia¹ Li Guan¹

4 ¹China Meteorological Administration Aerosol-Cloud and Precipitation Key
5 Laboratory, Nanjing University of Information Science and Technology, Nanjing
6 210044, China

7 Correspondence to: Li Guan liguan@nuist.edu.cn

8 **Abstract**

9 Cloud fraction as a vital component of meteorological satellite products plays an
10 essential role in environmental monitoring, disaster detection, climate analysis, and
11 other research areas. Random Forest(RF) and Multilayer Perceptron(MLP) algorithms
12 were used in this paper to retrieve the cloud fraction of AGRI (Advanced
13 Geosynchronous Radiation Imager) onboard FY-4A satellite based on its full-disc level-
14 1 radiance observation. Corrections has been made subsequently to the retrieved cloud
15 fraction in areas where solar glint occurs using a correction curve fitted with sun-glint
16 angle as weight. The algorithm includes two steps: the cloud detection is conducted
17 firstly for each AGRI field of view to identify whether it is clear sky, partly cloudy or
18 overcast within the observation field. Then the cloud fraction is retrieved for the scene
19 identified as partly cloudy. The 2B-CLDCLASS-LIDAR cloud fraction product from
20 Cloudsat& CALIPSO active remote sensing satellite is employed as the truth to assess
21 the accuracy of the retrieval algorithm. Comparison with the operational AGRI level 2
22 cloud fraction product is also conducted at the same time. The results indicate that both
23 the Random Forest (RF) and Multi-Layer Perceptron (MLP) cloud detection models
24 achieved high accuracy, surpassing that of operational products. However, both
25 algorithms demonstrated weaker discrimination capabilities for partly cloudy
26 conditions compared to clear sky and overcast situations. Specifically, they tended to
27 misclassify fields of view with low cloud fractions (e.g., cloud fraction = 0.16) as clear

28 sky and those with higher cloud fractions (e.g., cloud fraction = 0.83) as overcast.
29 Between the two models, RF exhibited higher overall accuracy. Both RF and MLP
30 models performed well in cloud fraction retrieval, showing lower mean error (ME),
31 mean absolute error (MAE), and root mean square error (RMSE) compared to
32 operational products. The ME for both RF and MLP cloud fraction retrieval models was
33 close to zero, while RF had slightly lower MAE and RMSE than MLP. During daytime,
34 the high reflectance in sun-glint areas led to larger retrieval errors for both RF and MLP
35 algorithms. However, after correction, the retrieval accuracy in these regions improved
36 significantly. At night, the absence of visible light observations from the AGRI
37 instrument resulted in lower classification accuracy compared to daytime, leading to
38 higher cloud fraction retrieval errors during nighttime.

39 **Key words:** Cloud detection; cloud fraction retrieval; FY-4A AGRI; CloudSat &
40 CALIPSO; machine learning; deep learning.

41 **Introduction**

42 Clouds occupy a significant proportion within satellite remote sensing data
43 acquired for Earth observation. According to the statistics from the International
44 Satellite Cloud Climatology Project (ISCCP), the annual average global cloud coverage
45 within satellite remote sensing data is around 66% with even higher cloud coverage in
46 specific regions (such as the tropics) (Zhang, et al., 2004). The impact of clouds on the
47 radiation balance of the Earth's atmospheric system is influenced by the optical
48 properties of clouds. Cloud detection, as a vital component of remote sensing image
49 data processing, is considered a critical step for the subsequent identification, analysis,
50 and interpretation of remote sensing images. Therefore, accurately determining cloud
51 coverage is essential in various research domains, such as environmental monitoring,
52 disaster surveillance and climate analysis.

53 Fengyun-4A (FY-4A) is a comprehensive atmospheric observation satellite

54 launched by China in 2016. The uploaded AGRI (Advanced Geosynchronous Radiation
55 Imager) has 14 channels and captures full-disk observation every 15 minutes. In
56 addition to observing clouds, water vapor, vegetation and the Earth's surface, it also
57 possesses the capability to capture aerosols and snow. Moreover, it can clearly
58 distinguish different phases and particle size of clouds and obtain high- to mid-level
59 water vapor content. It is particularly suitable for cloud detection due to its
60 simultaneous use of visible, near-infrared, and long-wave infrared channels for
61 observation with 4km spatial resolution.

62 Numerous cloud detection algorithms have been provided based on observations
63 from satellite-borne imagers. The threshold method has been widely employed by
64 researchers, including the early ISCCP (International Satellite Cloud Climatology
65 Project) method (Rossov, 1993) and the proposed threshold methods based on different
66 spectral features or underlying surfaces (Kegelmeyer,1994; Solvsteen,1995; Baum and
67 Trepte,1996). However, there is a significant subjectivity in selection of thresholds
68 whether it is the single and fixed threshold in the early days, multiple thresholds,
69 dynamic thresholds, or adaptive thresholds. The selection of thresholds is influenced
70 by season and climate. Surface reflectance varies significantly between different
71 seasons, such as increased reflectance from snow in winter and vegetation flourishing
72 in summer affecting reflectance. As a result, changes in surface features during different
73 seasons lead to variations in the distribution of grayscale values in images, requiring
74 adjustments to thresholds based on seasonal characteristics. Climate conditions like
75 cloud cover, atmospheric humidity, etc., impact the distinguishability of clouds and
76 other features. For instance, in humid or cloudy climates, the reflectance of the surface
77 and clouds may be similar, necessitating stricter thresholds for differentiation.
78 Therefore, climate conditions also influence threshold selection.

79 The other category of cloud detection algorithms is based on statistical probability
80 theory. For example the principal component discriminant analysis and quadratic

81 discriminant analysis methods were used to SEVIRI (Spinning Enhanced Visible and
82 Infrared Imager) cloud detection (Amato et al., 2008). The cloud detection algorithm
83 for Thermal Infrared (TIR) sensor was based on the Bayesian theory of total probability
84 (Merchant et al., 2010) and the naive Bayes algorithm for AGRI (Yan , et al., 2022).
85 The unsupervised clustering cloud detection algorithms for MERIS (Medium
86 Resolution Imaging Spectrometer) (GomezChova , et al., 2007) and the fuzzy C-means
87 clustering algorithms for MODIS (Pan, et al., 2009) all have achieved high accuracy in
88 cloud detection.

89 More and more machine learning algorithms are being utilized by researchers in
90 cloud detection studies with the development of machine learning. For instance, the
91 probabilistic neural networks, especially radial basis function networks was used for
92 AVHRR cloud detection (Zhang, et al., 2001). The utilization of convolutional neural
93 network methods (Chai, et al., 2024) offers important perspectives for cloud detection
94 research.

删除了: Hu

删除了: 2020

95 Currently, there is limited research literature on cloud detection and cloud fraction
96 retrieval algorithms for FY-4A/4B AGRI. The operational cloud fraction product of FY-
97 4A AGRI utilized a threshold method with 4 km spatial resolution. Differences in
98 climatic and environmental factors lead to varying albedo and brightness temperature
99 observations for the instrument at different times and locations. Therefore, the choice
100 of thresholds is easily influenced by factors such as season, latitude and land surface
101 type (Gao and Jing, 2019). Using multiple sets of thresholds for discrimination would
102 significantly slow down the cloud detection process. Moreover, most algorithms focus
103 solely on cloud detection, which classified the observed scenes into cloud or clear-sky
104 without providing the specific cloud fraction information for the scenes. The use of
105 active remote sensing instruments carried by Cloudsat & Calypso is not influenced by
106 thresholds when retrieving cloud fraction, enabling a more accurate cloud fraction
107 retrieval. However, due to Cloudsat & Calypso being polar-orbiting satellites, the cloud

110 fraction over the full disk cannot be obtained. Utilizing the Cloudsat & Calypso Level
111 2 product 2B-CLDCLASS-LIDAR as the reference truth, a random forest model trained
112 based on FY4A AGRI full disk radiation data can address the shortcomings of threshold
113 methods and achieve a high accuracy of cloud fraction over the full disk.

114 In summary, this paper established cloud detection and cloud fraction retrieval
115 models using a Multi-Layer Perceptron (MLP) and Random Forest (RF), based on FY-
116 4A AGRI full-disk level 1 observed radiance data. The cloud fraction from the CloudSat
117 & CALIPSO level 2 product 2B-CLDCLASS-LIDAR was used as the label. The results
118 were compared with the 2B-CLDCLASS-LIDAR product and the official AGRI
119 operational products for validation.

120 **1 Research Data and Preprocessing**

121 *1.1 FY-4A data*

122 FY-4A was successfully launched on December 11, 2016. Starting from May 25, 2017,
123 FY-4A drifted to a position near the main business location of the Fengyun
124 geostationary satellite at 104.7 degrees east longitude on the equator. Its successful
125 launch marked the beginning of a new era for China's next-generation geostationary
126 meteorological satellites as an advanced comprehensive atmospheric observation
127 satellite. The Advanced Geosynchronous Radiation Imager (AGRI), one of the main
128 payloads of the Fengyun-4 series geostationary meteorological satellites, can perform
129 large-disk scans and rapid regional scans at a minute level. It has 14 observation
130 channels in total with the main task of acquiring cloud images. The channel parameters
131 and main uses of AGRI are detailed in Table 1
132 (<https://www.nsmc.org.cn/nsmc/cn/instrument/AGRI.html>). The first six visible light
133 channels have no values at night, meaning that channels with a central wavelength less
134 than or equal to $2.225\mu\text{m}$ are unavailable during nighttime. FY-4A AGRI data was
135 downloaded from the official website of the China national satellite meteorological

136 center (<http://satellite.nsmc.org.cn>), including level-1 full disk radiation observation
 137 data preprocessed through quality control, geolocation and radiation calibration as well
 138 as level-2 cloud fraction product (CFR). The spatial resolution of these data is all 4 km
 139 at nadir and the temporal resolution is 15 minutes.

140 Table 1 FY-4A AGRI channel parameters

Channel Number	Band Range / μm	Central Wavelength / μm	Spatial resolution/km	Main Applications
1	0.45 ~ 0.49	0.47	1	clouds, dust, aerosols
2	0.55 ~ 0.75	0.65	0.5	clouds, sand dust, snow
3	0.75 ~ 0.90	0.825	1	vegetation
4	1.36 ~ 1.39	1.375	2	cirrus
5	1.58 ~ 1.64	1.61	2	clouds, snow
6	2.10 ~ 2.35	2.225	2	cirrus, aerosols
7	3.50 ~ 4.00	3.75H	2	fire point, the intense solar reflection signal
8	3.50 ~ 4.00	3.75L	4	low clouds, fog
9	5.80 ~ 6.70	6.25	4	upper-level water vapor
10	6.90 ~ 7.30	7.1	4	mid-level water vapor
11	8.00 ~ 9.00	8.5	4	subsurface water vapor
12	10.30 ~ 11.30	10.8	4	surface and cloud-top temperatures
13	11.50 ~ 12.50	12.0	4	surface and cloud-top temperatures
14	13.2 ~ 13.8	13.5	4	cloud-top height

删除了: 13

141 **1.2 CloudSat & Calipso Cloud Product**

142 CALIPSO (Cloud-Aerosol Lidar and Infrared Pathfinder Satellite Observations)
 143 is a satellite jointly launched by NASA and CNES (the French National Center for
 144 Space Studies) in 2006. It is a member of the A-Train satellite observation system.
 145 CALIPSO is equipped with three payloads, among which CALIOP (the Cloud and
 146 Aerosol Lidar with Orthogonal Polarization) is a primary observational instrument.
 147 Observing with dual wavelengths (532 nm and 1064 nm) CALIOP can provide high-
 148 resolution vertical profiles of clouds and aerosols with 30 m vertical resolution. As the
 149 first satellite designed to observe global cloud characteristics in a sun-synchronous orbit
 150 CloudSat is also among NASA's A-Train series satellites. The CPR (Cloud Profile
 151 Radar) installed on it operates at 94 GHz millimeter-wave and is capable of detecting
 152 the vertical structure of clouds and providing vertical profiles of cloud parameters. The

154 scanning wavelengths of CPR and CALIOP are different. CALIOP is capable of
155 observing the top of mid-to-high level clouds, whereas CPR can penetrate optically
156 thick clouds. Combining the strengths of these two instruments enables the acquisition
157 of precise and detailed information on cloud layers and cloud fraction.

158 The joint level 2 product 2B-CLDCLASS-LIDAR is mainly utilizing in this study.
159 It provides the cloud fraction at different heights with horizontal resolution 2.5 km
160 (along-track) \times 1.4 km (cross-track) through combining the observations from CPR and
161 CALIOP. Since the two instruments have different spatial domain such as vertical
162 resolution, spatial resolution and spatial frequency, the spatial domain of the output
163 products is defined in terms of the spatial grid of the CPR. In the algorithm, the cloud
164 fraction is calculated using a weighted scheme based on the spatial probability of
165 overlap between the radar and lidar observations. The calculation of the lidar cloud
166 fraction within a radar footprint is represented by the equation 1 (Mace, G. G., et al,
167 2007):

$$168 \quad C_l = \frac{\sum_{i=1}^{\# \text{ of lidar obs}} w_i \delta_i}{\sum_{i=1}^{\# \text{ of lidar obs}} w_i} \quad (1)$$

169 Where:

170 C_l represents the lidar cloud fraction within a radar footprint.

171 w_i is the spatial probability of overlap for a particular lidar observation.

172 δ_i indicates the lidar hydrometeor occurrence, where a value of 1 signifies the
173 presence of hydrometeor and 0 indicates the absence.

174 i counts the lidar profile in a specific radar observational domain.

175 This calculation considers the contributions of multiple lidar observations within
176 a radar resolution volume to determine the cloud fraction within that volume. The
177 CloudSat product manual (Wang, 2019) can be referred for more detailed information
178 on 2B-CLDCLASS-LIDAR. The data used is available to download from the ICARE
179 data and services center ([https://www.icare.univ-lille.fr/data-access/data-archive-
180 access/](https://www.icare.univ-lille.fr/data-access/data-archive-access/)).

181 ***1.3 Establishment of Training Data***

182 The crucial aspect of establishing a training data in machine learning algorithms
183 is how to obtain the cloud fraction values (ground truth) as labels. The error in cloud
184 fraction retrieved solely from passive remote sensing instruments is significant. Using
185 active remote sensing data can provide more accurate cloud fraction information in the
186 vertical direction. Therefore, the spatiotemporally matched 2B-CLDCLASS-LIDAR
187 cloud fraction are utilized as output labels in this paper.

188 The FY-4A AGRI and 2B-CLDCLASS-LIDAR data with a spatial difference
189 between fields of view within 1.5 km and a time difference within 15 minutes are
190 spatiotemporal matched. To make the 2B-CLDCLASS-LIDAR cloud fraction data
191 collocated within AGRI pixels more effective, at least two 2B-CLDCLASS-LIDAR
192 pixels are required within each AGRI field of view. The cloud fraction average of these
193 pixels is used as the cloud fraction for that AGRI pixel. However, the errors in the
194 matched dataset are unavoidable. The AGRI scanning method operates from left to right
195 and top to bottom. Each complete scan of the full disk takes 15 minutes and generates
196 a dataset. It is impossible to determine the exact moment of a specific point within the
197 full disk. This limits the time range for matching datasets to within 15 minutes.
198 However, in areas with higher wind speeds, clouds can move a significant distance
199 within that 15-minute window. Therefore, errors arising from timing issues cannot be
200 avoided.

201 Cloud detection and cloud fraction label generation for 2B-CLDCLASS-LIDAR
202 are as follows. There may be multiple layers of clouds in each field of view. If there is
203 at least one layer cloud with cloud fraction of 1 in the 2B-CLDCLASS-LIDAR profile,
204 then the scene is labeled as overcast with a cloud fraction of 1. If all layers in the profile
205 are cloud-free, the scene is labeled as clear sky. The scene between the above two
206 situations is labeled as partly cloudy and the cloud fraction is the average of cloud
207 fractions at different layers.

208 The algorithm includes two steps: the cloud detection is conducted firstly for each
209 AGRI field of view to identify whether it is clear sky, partly cloudy or overcast within
210 the observation field. Then the cloud fraction is retrieved for the scene identified as
211 partly cloudy. So the training data include dataset A used for cloud detection and dataset
212 B for cloud fraction retrieval. The input variables in dataset A are the FY-4A AGRI
213 level-1 radiative observations from 14 channels and the output variable is the
214 temporally and spatially matched 2B-CLDCLASS-LIDAR cloud detection label. The
215 output is categorized into three types: overcast, partly cloudy and clear sky with values
216 1, 2 and 3 respectively. The cloud fraction product from 2B-CLDCLASS-LIDAR
217 consists of discrete values: 0, 0.16, 0.33, 0.50, 0.66, 0.83, and 1. According to the result
218 statistics, the cloud fractions of 2B-CLDCLASS-LIDAR pixels within the AGRI field
219 of view are mostly the same. After averaging, the proportions of cloud fractions of [0.16,
220 0.33, 0.5, 0.67, 0.83] are extremely high. Therefore, other cloud fraction situations with
221 extremely small proportions can be ignored. Doing so can also better balance the
222 training samples. Here, 0 indicates clear sky, values from 0 to 1 represent varying cloud
223 fractions for partly cloudy conditions, and 1 signifies overcast. To ensure the balance
224 and representativeness of the samples, the proportions of different cloud fraction
225 samples in dataset A are set at 5:1:1:1:1:5. Regarding the samples for partly cloudy
226 type in dataset A, the collocated 2B-CLDCLASS-LIDAR cloud fraction products serve
227 as output labels for cloud fraction retrieval model B. The input of training dataset B
228 remains the FY-4A AGRI level-1 radiative observations.

229 Due to the instrument's limited lifespan, only 2B-CLDCLASS-LIDAR data up to
230 August 2019 can be obtained. The sample time range used in this paper is from August
231 2018 to July 2019. Five days were randomly selected each month as daytime samples
232 and five days as nighttime samples. A total of 120 days of time and space matched FY-
233 4A AGRI full-disk observations and 2B-CLDCLASS-LIDAR data were used as
234 training and testing samples. Among them, 80% of the data was used for training, and

删除了: A

删除了: B

删除了: A

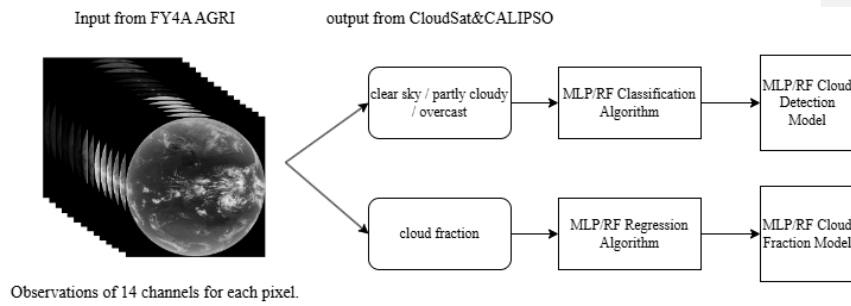
238 20% was used for testing. The total number of daytime samples in dataset A is 91,073,
239 while dataset B contains 30,358 samples. The total number of nighttime samples in
240 dataset A is 95,493, and dataset B includes 31,831 samples.

241 Although the model was trained and tested using data from 2018 to 2019, to test
242 the universality of the algorithm, it was applied to real-time observations from FY-4A
243 and FY-4B AGRI in 2023.

244 2 Algorithms

245 Our preliminary experiments involved multiple algorithms, including LibSvm,
246 MLP, BP neural network, and Random Forest. These experiments highlighted that,
247 among the baselines, Random Forest and MLP achieved the highest overall accuracy.

248 For this reason, we selected them to perform additional experiments. Using RF and
249 MLP algorithms to train the model with the established sample set, the overall process
250 is shown in the Figure 1.



251 Observations of 14 channels for each pixel.

252 **Figure 1: Method workflow.** The input consists of 14 channel observation values
253 for each pixel from FY4A AGRI, and the ground truth labels or outputs are sourced
254 from the CloudSat&CALIPSO cloud fraction products. The cloud detection
255 classification model and the cloud fraction retrieval model are established separately.

256 2.1 Random Forest (RF)

257 This algorithm integrates multiple trees based on the Bagging idea of ensemble
258 learning, with the basic element being the decision tree (Breiman, 1999). When building

259 a decision tree, N sets of independent and dependent variables are randomly sampled
260 with replacement from the original training samples to create a new training sample set;
261 m variables are randomly sampled without replacement from all independent variables,
262 the dependent variable data is split into two parts using the selected variables, and the
263 purity of the subsets is calculated for each split method. The variable utilized by the
264 split method with the highest purity is used to partition the data, completing the decision
265 at that node. This process of binary splitting continues to grow the decision tree until
266 stopping criteria are met, completing the construction of a single decision tree. These
267 steps are repeated N_{tree} times to build a random forest model consisting of N_{tree}
268 decision trees (Breiman, 2001). Random Forest adopts ensemble algorithms, with the
269 advantage of high accuracy. It can handle both discrete and continuous data, without
270 the need for normalization, making it more efficient compared to other algorithms.

271 **2.2 Multilayer Perceptron (MLP)**

272 This algorithm consists of a fully connected artificial neural network (Duda, et al.,
273 2001). The classifier/regressor takes feature vectors or tensors as input. The input is
274 mapped through multiple fully connected hidden layers containing hidden weights,
275 which produce classifications/regressions at the output layer. A nonlinear activation
276 function (such as sigmoid or rectified linear unit (ReLU)) is applied in each hidden
277 layer to facilitate a nonlinear model. For classifiers, the output of the final hidden layer
278 is combined and passed through a softmax function to generate class predictions. For
279 the loss function, the cloud detection model is cross-entropy, and the cloud fraction
280 model is MSE. The model's weights are trained in a supervised manner using
281 backpropagation.

282 **2.3 Hyperparameters**

283 In this paper, a total of eight models were established, including daytime/nighttime

删除了: The model's weights are trained in a supervised manner, utilizing stochastic gradient descent and backpropagation to achieve the desired classification/regression....

288 random forest classification/regression models and daytime/nighttime MLP
 289 classification/regression models. For the random forest, we first conducted experiments
 290 using the following Hyperparameters ranges: Trees: [200, 300, 400, 500, 600,700],
 291 minleaf: [1, 2, 5, 10], criterion: [Gini, entropy]. Ultimately, the best selections were: (1)
 292 Daytime RF classification model: Trees=500, (2) Nighttime RF classification model:
 293 Trees=600, (3) Daytime RF regression model: Trees=400, (4) Nighttime RF regression
 294 model: Trees=500, All four models have minleaf=1, criterion=gini.

295 For the MLP, experiments were conducted using the following hyperparameter
 296 ranges: Number of hidden layers: [2,3,4,5,6,7,8,9], Hidden layer size: [8,16,32,64,128],
 297 Epochs: [30,50,100], Solver hyperparameter: [lbfgs, sgd, adam]. The optimal
 298 parameters found are as follows: (1) MLP classification model for daytime: number of
 299 hidden layers = 5, (2) MLP classification model for nighttime: number of hidden layers
 300 = 5, (3) MLP regression model for daytime: number of hidden layers = 4, (4) MLP
 301 regression model for nighttime: number of hidden layers = 6. All four models have
 302 Hidden layer size = 64, Epochs = 50, solver = adam, BatchSize = 1500, Initial learning
 303 rate = 0.01, Learning rate schedule = piecewise, Factor for dropping the learning rate =
 304 0.1, Number of epochs for dropping the learning rate = 10.

305 3 Results and Analysis

306 To assess the accuracy and stability of the retrieval model, two types of validation
 307 methods are utilized. One way involves a direct comparison from images, qualitatively
 308 comparing the model's retrieval results and official cloud fraction products with AGRI
 309 observed cloud images. Another approach uses 2B-CLDCLASS-LIDAR as the ground
 310 truth and introduces five parameters for quantitative comparison: recall, false alarm rate
 311 (FAR), mean error (ME), mean absolute error (MAE), and root mean square error
 312 (RMSE). To evaluate the ability of operational products, RF, and MLP cloud detection
 313 models to distinguish overcast, partly cloudy, and clear sky, the recall is calculated using

- 删除了: , minleaf=1, criterion=gini;
- 删除了: , minleaf=1, criterion=gini;
- 删除了: , minleaf=1, criterion=gini;
- 删除了: ,
- 删除了: minleaf=1, criterion=gini.
- 删除了: Hidden layer size
- 删除了: neuron count
- 删除了: Activation hyperparameter: [logistic, tanh, relu], Max...
- 删除了: MiniBatchSize: [300,400,...,1500,1600],
- 删除了: hidden layer size
- 删除了: , MiniBatchSize = 1500
- 删除了: hidden layer size
- 删除了: , MiniBatchSize = 800
- 删除了: hidden layer size
- 删除了: , MiniBatchSize = 600
- 删除了: hidden layer size
- 删除了: , MiniBatchSize = 500
- 删除了: hidden layer neuron count
- 删除了: activation = relu, Max
- 删除了: InitialLearnRate
- 删除了: LearnRateSchedule
- 删除了: LearnRateDropFactor
- 删除了: LearnRateDropPeriod

338 the formula $POD=TP/(TP+FN)$, and the false alarm rate is calculated using the formula
339 $FAR=FP/(TP+FP)$. Taking the overcast scene as an example, TP represents the number
340 of correctly identified overcast conditions, FN represents the number of overcast
341 conditions misidentified as partly cloudy or clear sky, and FP represents the number of
342 clear sky or partly cloudy conditions misidentified as overcast. When assessing the
343 accuracy of operational products and cloud fraction models for the cloud fraction
344 retrieval results of partly cloudy scenes, mean error (ME), mean absolute error (MAE),
345 and root mean square error (RMSE) are used.

346 3.1 Objective Analysis of Cloud Fraction Retrievals

347 First, using the 2B-CLDCLASS-LIDAR cloud fraction product as the ground truth,
348 we calculated the accuracy of the operational cloud detection products. The results are
349 shown in columns 3-4 of Table 2. The samples used for this statistic are the same as
350 those for testing the model below (20% of dataset A).

351 Based on the cloud detection model trained above, cloud detection experiments
352 were conducted using the test samples from dataset A. The time-space matched 2B
353 CLDCLASS-LIDAR cloud fraction product served as the ground truth to assess the
354 accuracy of cloud detection. The results are shown in columns 5-8 of Table 2. During
355 the day, the Random Forest model achieved an overall accuracy of 94.2%, while the
356 MLP model had an overall accuracy of 93.7%. The Random Forest model exhibited
357 slightly higher recall rates for clear skies, partly cloudy, and overcast conditions
358 compared to the MLP model, and its FAR was lower as well. Both models performed
359 poorly in recognizing partly cloudy conditions, as the models tended to classify true
360 cloud fractions of 0.16 as clear skies and those of 0.83 as overcast. At night, the Random
361 Forest model achieved an overall accuracy of 89.4%, while the MLP model had an
362 accuracy of 88.7%. The Random Forest model had higher recall rates for clear skies
363 and partly cloudy conditions compared to the MLP, while the recall rates for overcast

删除了: The results are shown in Table 2.

删除了: Table 2: Recall Rate and FAR of Operational Cloud Detection Products

删除了: D

删除了: Figure 1 shows the results: (a) Random Forest model results during the day, (b) MLP model results during the day, (c) Random Forest model results during the night, and (d) MLP model results during the night. The x-axis represents the model predictions, while the y-axis represents the ground truth. A value of 1 on both axes indicates clear skies, 2 indicates partly cloudy, and 3 indicates overcast. The blue area on the right side of each plot shows the recall rate for each type, while the light-colored area at the bottom represents the False Alarm Rate (FAR).

378 conditions were similar for both models. The FAR for the Random Forest model was
 379 lower than that of the MLP. Overall, both the Random Forest and MLP models showed
 380 higher classification accuracy for clear skies, partly cloudy, and overcast conditions
 381 compared to operational products, with the Random Forest model performing better.

382 Table 2: Recall Rate, FAR of Operational Cloud Detection Products and multiple
 383 models.

Classification	Daytime	Nighttime	Daytime	Nighttime	Daytime	Nighttime	
	Product	Product	RF	RF	MLP	MLP	
POD	Clear Sky	0.6359	0.5781	0.964	0.919	0.959	0.905
	Partly cloudy	0.7174	0.7449	0.914	0.845	0.895	0.808
	Overcast	0.7736	0.7384	0.959	0.919	0.957	0.920
FAR	Clear Sky	0.1778	0.0934	0.047	0.102	0.064	0.131
	Partly cloudy	0.1819	0.2117	0.078	0.153	0.085	0.172
	Overcast	0.2499	0.2683	0.038	0.061	0.039	0.063

384 Based on the previous model's assessment of the field of view as partly cloudy, the
 385 cloud fraction in this AGRI field of view is retrieved using the cloud fraction model
 386 established earlier. For model evaluation, both the operational product and the 2B-
 387 CLDCLASS-LIDAR cloud fraction product are classified as partly cloudy, with the
 388 matched 2B-CLDCLASS-LIDAR cloud fraction product considered as the ground truth.
 389 The average error, mean absolute error, and root mean square error for both daytime
 390 and nighttime operational products and cloud fraction model retrieval (Table 3) are
 391 calculated. It can be observed that the average errors of both models are close to 0
 392 during both daytime and nighttime. The errors are smaller during the day than at night,
 393 with the RF model exhibiting lower errors than the MLP model. In summary, the errors
 394 of both models are smaller than those of the operational products, and the RF model
 395 performs better in the cloud fraction retrieval task.

397 Table 3: Errors of Cloud Fraction

带格式的: 居中, 缩进: 首行缩进: 0 字符, 行距: 单倍行距

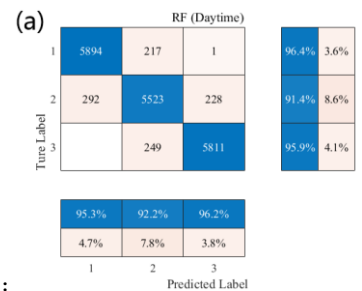
带格式的: 行距: 单倍行距

格式化表格

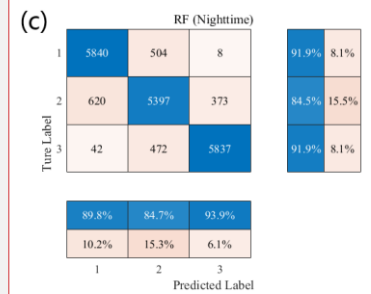
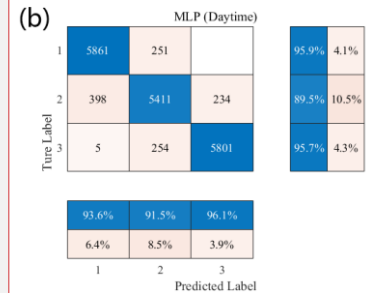
带格式的: 行距: 单倍行距

带格式的: 行距: 单倍行距

带格式的: 缩进: 首行缩进: 0 字符, 行距: 1.5 倍行距



删除了:



删除了: (Table 3)

删除了: 4

删除了: Operational Product

带格式的: 行距: 单倍行距

删除了:

Daytime Operational Product

	<u>Daytime</u>	<u>Nighttime</u>	<u>Daytime</u>	<u>Daytime</u>	<u>Nighttime</u>	<u>Nighttime</u>
	<u>Product</u>	<u>Product</u>	<u>RF</u>	<u>MLP</u>	<u>RF</u>	<u>MLP</u>
<u>ME</u>	<u>0.1987</u>	<u>0.2121</u>	<u>0.0006</u>	<u>-0.0009</u>	<u>-0.0028</u>	<u>-0.0032</u>
<u>MAE</u>	<u>0.2279</u>	<u>0.2441</u>	<u>0.1011</u>	<u>0.1053</u>	<u>0.1221</u>	<u>0.1322</u>
<u>RMSE</u>	<u>0.2776</u>	<u>0.2938</u>	<u>0.1285</u>	<u>0.1332</u>	<u>0.1510</u>	<u>0.1623</u>

删除了: Table 4:Model Retrieval Error

删除了:
Daytime RF

414

415

416

417

Based on the experiments mentioned above, the performance of RF in cloud detection and cloud fraction retrieval slightly outperforms that of MLP. Therefore, subsequent experiments will utilize the RF algorithm.

418

3.2 Cloud fraction correction in sun glint regions

419

420

421

422

423

424

425

Sun glint refers to the bright areas created by the reflection of sunlight to the sensors of observation systems (satellites or aircrafts). This phenomenon usually occurs on extensive water surfaces, such as oceans lakes or rivers. This specular reflection of sunlight will cause an increase in the reflected solar radiation received by onboard sensors, manifested as an enhancement of white brightness in visible images. The increase in visible channel observation albedo will affect various subsequent applications of data, including cloud detection and cloud cover retrieval, etc.

426

427

428

429

430

431

432

433

The position of Sun glint area can be determined using the SunGlintAngle value in the FY-4A GEO file. SunGlintAngle is defined as the angle between the satellite observation direction or reflected radiation direction and the mirror reflection direction on a calm surface (horizontal plane). It is generally accepted that the range of SunGlintAngle < 15° is easily affected by sun glint (Kay S, et al., 2009). The positions of the SunGlintAngle contour lines at 5 and 15° are marked in Figure 1(a). It can be observed that the edge of sun glint in Figure 1(a) essentially overlaps with the position of SunGlintAngle = 15°. Thus, the region where SunGlintAngle < 15° is defined as the

437 sun glint range in this paper and only the cloud fraction within this range will be
438 adjusted in the subsequent correction.

439 To correct the cloud fraction in the sun-glint areas, we first identified the fields of
440 view (FOVs) where sun-glint occurred during FY-4A AGRI observations from August
441 2018 to July 2019, totaling 1,476 FOVs. When matching the sample set of the sun glint
442 area, two issues need to be explained. 1) Cloud fraction is the average of cloud fractions
443 of different layers: Among the matched pixels, only one-layer cloud and two-layer
444 cloud appear. When there are two layers of cloud, there is always one layer with a cloud
445 fraction of 1. According to the previous description, when there is one layer with a cloud
446 fraction of 1, this pixel should be regarded as fully cloudy. 2) The average cloud fraction
447 of at least two CloudSat & CALIPSO pixels is taken as the cloud fraction of the AGRI
448 pixel: Due to the very small area of the sun glint area, the matching is very difficult. If
449 at least two CloudSat & CALIPSO pixels within an AGRI pixel are required, this will
450 make the available sample size very small. Therefore, when making the sample set of
451 the sun glint area, only one CloudSat & CALIPSO pixel within an AGRI pixel is
452 required. Due to the above two reasons, the true cloud fraction in the sample is a discrete
453 value. Subsequently, a direct least squares fitting was conducted between the retrieved
454 cloud fraction and the collocated 2B-CLDCLASS-LIDAR cloud fraction (ground truth).
455 The scatter plot is illustrated in Figure 2(b), where x-axis is the 2B-CLDCLASS-
456 LIDAR cloud fraction and y-axis is the model-retrieved cloud fraction. The blue line
457 represents the curve (namely Eq.2) fitted by the least squares method between the
458 retrievals and the truths. The thin dash line is the $x=y$ line. It is evident that the retrieved
459 cloud fraction is generally slightly overestimated.

460 Taking observations at 04:00 on 5 June 2019 as an example, Figure 2(c) presents
461 the distribution of SunGlintAngle and the flight trajectory of the Cloudsat&Calypso
462 satellite. White circles denote the sun glint region with SunGlintAngle $< 15^\circ$ and the
463 white line represents the satellite flight track. As depicted in the figure, the majority of

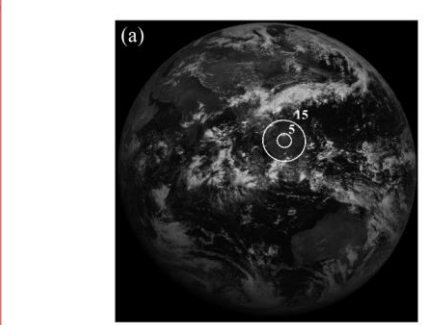
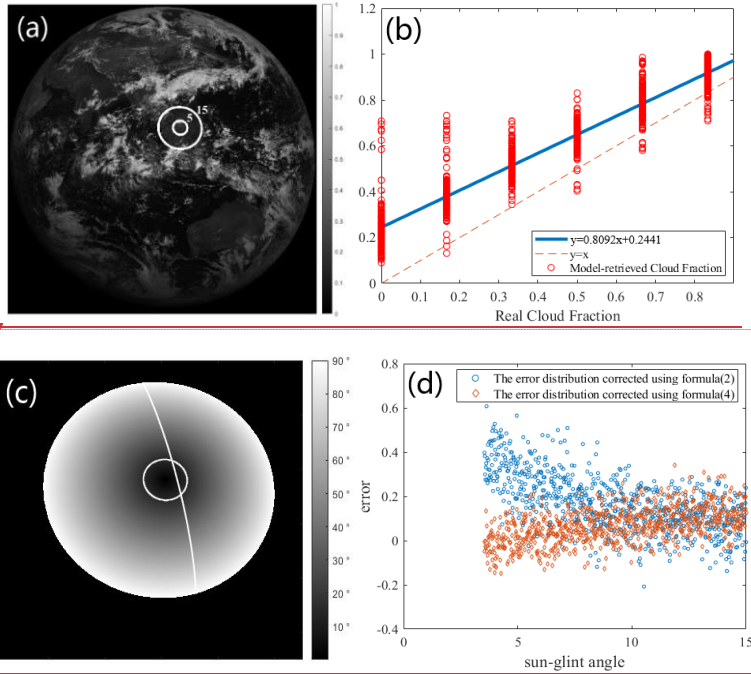
464 Cloudsat&Calypso flight trajectories do not pass through the central position of sun
465 glint area but instead traverse locations with larger SunGlintAngle values. The
466 intensity of sun glint effect decreases with the increase of SunGlintAngle. This
467 suggests that the true values for spatial and temporal matching mostly do not fall within
468 the strongest sun glint region. From Figure 2(d), it can be seen that the impact of sun
469 glint becomes stronger as SunGlintAngle decreasing, which results in a higher
470 observation albedo. This further leads to the overestimated cloud fraction values in the
471 retrieval. It is evident that the cloud fraction error is related to the value of
472 SunGlintAngle and this influence is not considered in Eq. (2). Directly applying
473 equation (2) to correct the cloud fraction retrievals would result in a too small correction
474 intensity for the FOVs near the center of sun glint and an excessively large correction
475 intensity for the FOVs in the Sun-glint edge region (even erroneous clear sky may
476 appear). Considering this, a correction formula (3)-(4) using SunGlintAngle as weight
477 is introduced, where W_i represents the angle weight for a certain pixel i in the sun glint
478 region, n is the number of pixels within the SunGlintAngle $< 15^\circ$ range, y_i is the initial
479 model retrieval of cloud cover for the field of view i and x_i is the final corrected cloud
480 fraction.

$$481 \quad x = (y - 0.2441)/0.8092 \quad (2)$$

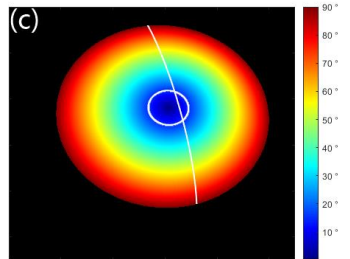
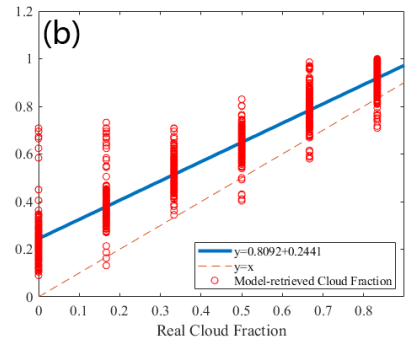
$$482 \quad W_i = \frac{glintangle_i}{\frac{1}{n} \sum_{i=0}^n glintangle_i} \quad (3)$$

$$483 \quad x_i = W_i \left(\frac{y_i - 0.2441}{0.8092} \right) \quad (4)$$

484 Figure 2(d) shows the distribution of errors with respect to SunGlintAngle,
485 where the blue dots represent the error distribution corrected using formula
486 (2), and the orange dots represent the error distribution corrected using
487 formula (4). It can be seen from Figure 2(d) that after correction by formula
488 (4), the errors in the smaller range of SunGlintAngle are significantly reduced.



删除了:



带格式的: 行距: 单倍行距

带格式的: 行距: 1.5 倍行距

489

490

491 **Figure 2:** (a) albedo image of 0.67 μ m channel (the circles are the contours of the sun-
 492 glint angle), (b) Scatter plot of cloud fraction in sun glint region (The blue line
 493 represents the curve (namely Eq.2) fitted by the least squares method between the
 494 retrievals and the truths.), (c) Distribution of SunGlintAngle and satellite flight track of
 495 CloudSat & Calypso at 4:00 on June 5, 2019, (d) Distribution of cloud fraction retrieval
 496 error with sun-glint angle.

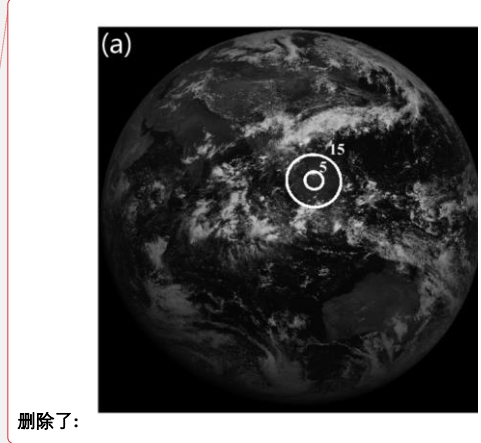
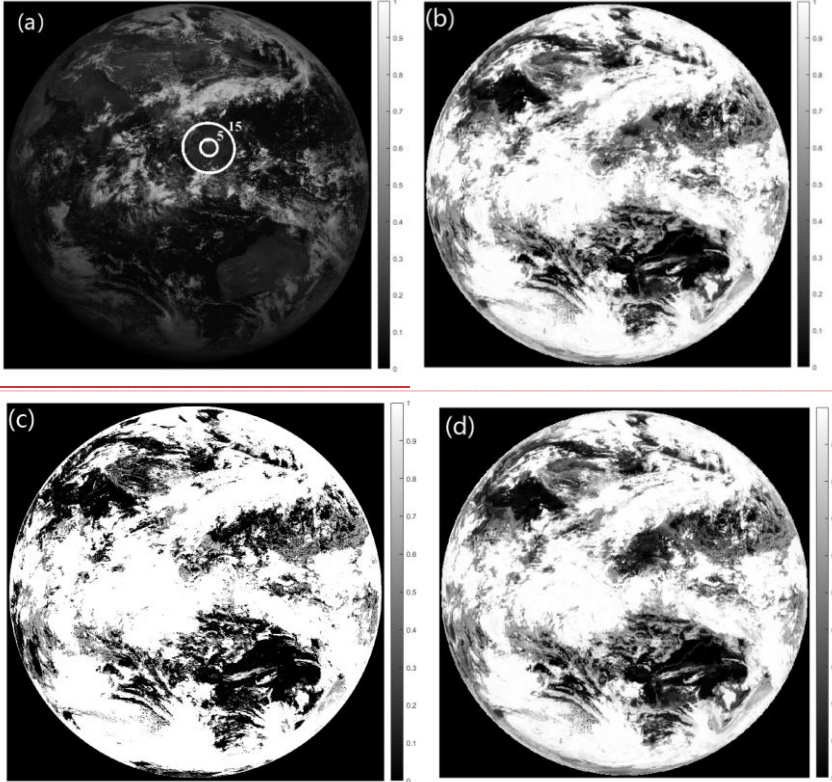
497 **3.3 Algorithm universal applicability testing**

498 Although the retrieval model in this article was built based on data from May 2019
 499 due to the limited lifespan of the instrument, how effective is it in real-time FY-4A
 500 AGRI observations and even subsequent FY-4B AGRI applications? The algorithm's
 501 universal applicability was tested using real-time observations from FY-4A and FY-4B
 502 AGRI in 2023.

503 Taking the full-disk observation of FY-4A AGRI at 04:00 (UTC, the same below)
 504 on 1 June 2023 as an example, the radiance observations from 14 channels are initially

512 fed into the random forest cloud detection model to determine the sky classification
513 (overcast, partly cloudy or clear sky) in each AGRI field. The random forest cloud
514 fraction retrieval model is utilized to retrieve the cloud fraction in scenes identified as
515 partly cloudy. Figure 3(a) is the observed albedo at $0.67\ \mu\text{m}$, where the circles represent
516 the contours of the sun glint angle, (b) is the cloud fraction retrievals from random forest
517 algorithm, (c) is the official operational cloud fraction product and (d) is random forest
518 cloud fraction retrievals with sun-glinton correction. It can be seen from Figure 3 that
519 many clear-sky scenes are erroneously identified as cloudy by the operational product
520 and the cloud fraction is generally overestimated with many scenes having a cloud
521 fraction of 1. The random forest algorithm identifies more regions as clear skies or
522 partly cloudy than the operational products, matching better with the observations in
523 the $0.67\ \mu\text{m}$ albedo image. Brighter regions in the visible image correspond to cloud
524 cover areas and darker areas represent clear sky conditions. The sun glint region in the
525 central South China Sea (the circled area in Figure 3(a)) is depicted in Figure 3(b),
526 where the clear-sky scenes over the ocean are misidentified as partly cloudy by random
527 forest algorithm due to the increase in observed albedo. Although operational product
528 in this area also suffers from the impact of unremoved sun glint, it identifies more clear-
529 sky scenes and the cloud fraction is relatively low. Thus, it is evident that the random
530 forest algorithm exhibits significant cloud detection and cloud fraction errors in these
531 sun glint regions. Correction is necessary for the cloud fraction retrievals in the sun
532 glint region.

533 Figure 3(d) shows the cloud fraction distribution after correction using equation
534 (9) in the sun glint region. The correction eliminates the influence of sun glint
535 comparing to the cloud fraction in sun glint area before correction in Figure 3(b). The
536 scenes misjudged as partly cloudy are corrected to clear sky and match well with the
537 actual albedo observations in 3(a), which accurately restores the true cloud coverage
538 over the South China Sea.



539

540

541 **Figure 3:** FY-4A AGRI at 04:00 on 1 June 2023 (a) albedo image of $0.67\mu\text{m}$ channel
 542 (the circles are the contours of the sun-glint angle), (b) random forest cloud fraction
 543 retrieval without sun-glint correction, (c) operational cloud fraction product, (d) random
 544 forest cloud fraction retrieval with sun-glint correction.

545 Statistical analysis was conducted on the correction effect using samples with sun
 546 glint in the training data. The POD and FAR in sun glint area is listed in table 5 and the
 547 error is in table 6. It can be seen that after correcting for cloud fraction, the POD for
 548 clear skies has increased from 0.0987 to 0.9023. The FAR for partly cloudy has
 549 decreased from 0.7943 to 0.0276. Both ME, MAE, and RMSE show significant
 550 reductions, and the results after correction outperform operational products.

551

Table 5 POD and FAR of Cloud Detection in sun glint area

Sky Classification	Operational Product	RF	RF after Correction
--------------------	---------------------	----	---------------------

	Clear Sky	0.4120	0.0987	0.9023
POD	Partly cloudy	0.7371	0.9663	0.9587
	Overcast	0.8856	0.9845	0.9845
	Clear Sky	0.1229	0.1633	0.0938
FAR	Partly cloudy	0.3332	0.7943	0.0276
	Overcast	0.2983	0.1321	0.1321

553

554

Table 6 cloud fraction Errors in sun glint area

	Operational Product	RF Retrievals	RF after Correction
ME	0.2354	0.1741	0.0670
MAE	0.2511	0.1820	0.0849
RMSE	0.2771	0.2166	0.1041

555

556

557

558

559

560

561

562

563

564

565

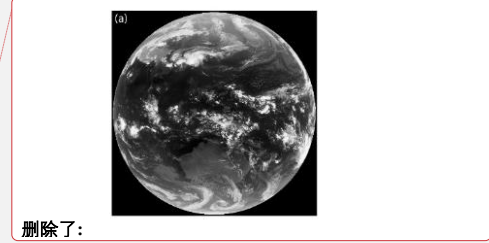
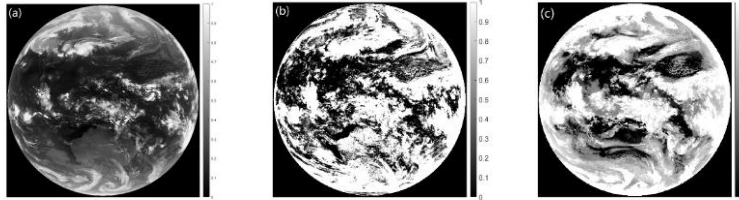
566

567

568

569

FY-4B launched in 2021 has a total of 15 channels with an additional low-level water vapor channel at 7.42 μm compared to FY-4A. Taking the full-disk observation of FY-4B AGRI at 17:00 on April 18, 2023, as an example, The radiance observation data of the remaining eight channels (near-infrared and infrared channels) except for the 7.42 μm channel and the visible light channels were input into the random forest cloud detection model. Figure 4 (a) shows the brightness temperature distribution observed in the 10.8 μm channel of FY-4B AGRI, (b) represents the operational cloud fraction product for FY-4B AGRI and (c) shows the cloud fraction retrieved by this algorithm. Figure 4 illustrates that the random forest algorithm identifies more regions as clear skies or partly cloudy than the operational products, aligning better with the brightness temperature observations in 10.8 μm . Especially in high latitude regions of the southern hemisphere and areas with strong convection near the equator, the cloud cover provided by operational products is too high and even misjudged. It can be seen that the random forest algorithm is also suitable for cloud fraction retrieval of FY-4B AGRI.



570
 571 **Figure 4:** FY-4B AGRI at 17:00 on 18 April 2023, (a) brightness temperature of 10.8 μ m
 572 channel, (b) operational cloud fraction product, (c) random forest cloud fraction
 573 retrieval.

574 **4 Conclusion**

575 This paper used the random forest and multi-layer perceptron (MLP) algorithms
 576 to retrieve cloud fraction from FY-4A AGRI full-disk Level-1 radiance observation data,
 577 and verified the accuracy of the algorithms using the Cloudsat & Calypso active remote
 578 sensing satellite's 2B CLDCLASS-LIDAR cloud fraction product. The following
 579 conclusions were drawn:

580 (1) The random forest and MLP algorithms performed well in cloud detection and
 581 cloud fraction retrieval tasks, and their accuracy was higher than that of operational
 582 products. The accuracy of cloud detection can reach over 93%, and the error of cloud
 583 fraction retrieval is close to zero. Compared with the MLP algorithm, the RF algorithm
 584 has a slightly higher accuracy in cloud detection, and a slightly lower error in cloud
 585 fraction retrieval, showing better performance.

586 (2) At night, the classification accuracy is lower than during the day due to the lack
 587 of observations in the visible channel of AGRI, resulting in higher cloud fraction errors
 588 at night.

589 (3) The accuracy of identifying partly cloudy scenes is lower than that of
 590 identifying clear sky and overcast scenes for both RF and MLP algorithms. Scenes with
 591 very low cloud fraction (0.16) are often misclassified as clear sky, while scenes with
 592 high cloud fraction (0.83) are often misclassified as overcast.

594 (4) The sun-glint area cloud fraction correction curve, fitted with SunGlintAngle
595 as the weight, greatly improves the accuracy of cloud fraction retrieval and reduces the
596 misclassification rate of clear sky scenes as partly cloudy or partly cloudy scenes as
597 overcast due to increased reflectance.

598

599 *Data availability*

600 FY-4A AGRI data is available at <http://satellite.nsmc.org.cn> and the 2B-CLDCLASS-
601 LIDAR data at <https://www.icare.univ-lille.fr/data-access/data-archive-access/>

602

603 *Author contributions*

604 JX: Formal analysis, Methodology, Software, Visualization and Writing – original draft
605 preparation. LG: Conceptualization, Data curation, Funding acquisition, Supervision,
606 Validation and Writing – review & editing.

607

608 *Competing interests*

609 The contact author has declared that none of the authors has any competing interests.

610

611 *Disclaimer*

612 *Acknowledgements*

613 Funding: This work was supported by the National Natural Science Foundation of
614 China under grant no. 41975028.

615 *We acknowledge the High Performance Computing Center of Nanjing University of*
616 *Information Science & Technology for their support of this work.*

617 **References**

618 Amato, U., Antoniadis, A., Cuomo, V., Cuttillo, L., Franzese, M., Murino, L., Serio,
619 C.: Statistical cloud detection from SEVIRI multispectral images, *Remote Sensing of*
620 *Environment*, 112, 750–766, <https://doi.org/10.1016/j.rse.2007.06.004>, 2008.

621 Baum, B., Trepte Q.: A Grouped Threshold Approach for Scene Identification in
622 AVHRR Imagery, *Journal of Atmospheric & Oceanic Technology*, 16, 793-800,
623 [https://doi.org/10.1175/1520-0426\(1999\)016<0793:AGTAFS>2.0.CO;2](https://doi.org/10.1175/1520-0426(1999)016<0793:AGTAFS>2.0.CO;2), 1999.

624 Breiman L.1999. Random Forests-Random Features [J]. *Machine Learning*.45(1): 5-32.
625 Breiman, L. Random Forests. *Machine Learning* **45**, 5–32 (2001).
626 doi.org/10.1023/A:1010933404324

627 [Chai D ,Huang J ,Wu M , et al.Remote sensing image cloud detection using a shallow](#)
628 [convolutional neural network\[J\].ISPRS Journal of Photogrammetry and Remote](#)
629 [Sensing,2024,20966-84.](#)

630 Merchant, C.J., Harris, A.R., Maturi, E., Maccallum S.: Probabilistic physically based
631 cloud screening of satellite infrared imagery for operational sea surface temperature
632 retrieval, *Quarterly Journal of the Royal Meteorological Society*, 131, 2735-2755,
633 <https://doi.org/10.1256/qj.05.15>, 2005.

634 Gao, J., Jing, Y.: Satellite Remote Sensing Cloud Detection Method Based on Fully
635 Convolutional Neural Network,*Infrared Technology*, 41, 607-615, 2019.

636 Gomez-Chova, L., Camps-Valls, G., Amoros-Lopez, J., Guanter, L., Alonso, L., Calpe,
637 J., Moreno, J.: New Cloud Detection Algorithm for Multispectral and Hyperspectral
638 Images: Application to ENVISAT/MERIS and PROBA/CHRIS Sensors, *IEEE*
639 *International Symposium on Geoscience and Remote Sensing*, 2757–
640 2760, doi:10.1109/igarss.2006.709, 2006.

641 Kay, S., Hedley, J., Lavender, S.: Sun Glint Correction of High and Low Spatial
642 Resolution Images of Aquatic Scenes: a Review of Methods for Visible and Near-
643 Infrared Wavelengths, *Remote Sensing*, 1, 697-730,
644 <https://doi.org/10.3390/rs1040697>, 2009.

645 Kegelmeyer, W.P.J.: Extraction of cloud statistics from whole sky imaging
646 cameras,1994.

647 Kong, Y.-L., Huang, Q., Wang, C., Chen, J., Chen, J., & He, D. (2018). Long Short-
648 Term Memory Neural Networks for Online Disturbance Detection in Satellite Image
649 Time Series. *Remote Sensing*, 10(3), 452. doi:10.3390/rs10030452

650 Mace, G. G., R. Marchand, Q. Zhang, et al. (2007). CloudSat Project: Level 2 Radar-
651 Lidar GEOPROF product process description and interface control document. Jet
652 Propulsion Laboratory.

653 Pan, C., Xia B., Chen, Y.: Research on MODIS Cloud Detection Algorithms Based on
654 Fuzzy Clustering, *Microcomputer Information*, 25, 124-125+131, 2009.

655 Yan J, Guo X, Qu J, Han M. An FY-4A/AGRI cloud detection model based on the naive
656 Bayes algorithm. *Remote Sensing for Natural Resources*, 34(3): 33-42. doi:
657 10.6046/zrzyyg.2021259. 2022

658 Rossow, W. B., Leonid, C.G.: Cloud detection using satellite measurements of infrared
659 and visible radiances for ISCCP. *Journal of Climate*, 12, 2341-2369,
660 [https://doi.org/10.1175/1520-0442\(1993\)006<2341:CDUSMO>2.0.CO;2](https://doi.org/10.1175/1520-0442(1993)006<2341:CDUSMO>2.0.CO;2), 1993.

661 R.O. Duda, P.E. Hart, and D.G. Stork, *Pattern Classification*, New York: John Wiley &

删除了:

Hu, J.: Research on Cloud Detection Algorithm of Remote Sensing Image Based on Convolution Neural Network, *Nanjing University of Information Science and Technology*. doi:10.27248/d.cnki.gnjqc.2020.000625, 2020.

667 Sons, 2001, pp. xx + 654, ISBN: 0-471-05669-3. *Journal of Classification* 24, 305–
668 307 (2007). <https://doi.org/10.1007/s00357-007-0015-9>
669 Solvsteen, C.: Correlation based cloud-detection and an examination of the split-
670 window method, *Proceedings of SPIE - The International Society for Optical*
671 *Engineering*, 86-97, 1995.
672 Wang, Z.: CloudSat Project: CloudSat 2B-CLDCLASS-LIDAR product process
673 description and interface control document, *Jet Propulsion Laboratory*, 2019.
674 Yan, J., Guo, X., Qu, J.: An FY-4A/AGRI cloud detection model based on the naive
675 Bayes algorithm, *Remote Sensing for Natural Resources*, 34, 33-42, 2022.
676 Zhang, W., He, M., Mak, M.W.: Cloud detection using probabilistic neural networks,
677 *Geoscience and Remote Sensing Symposium*, IEEE 2373-2375, 2001.
678 Zhang, Y., William, B. R., Andrew, A. L., Valdar, O., Michael, I. M.: Calculation of
679 radiative fluxes from the surface to the top of atmo- sphere based on ISCCP and other
680 global data sets: Refine- ments of the radiative transfer model and the input data,
681 *Journal of Geophysical Research Atmospheres*, 109, 1-27,
682 <https://doi.org/10.1029/2003JD004457>, 2004.